LAWRENCE
LIVERMORE
NATIONAL
LABORATORY

LLNL-JRNL-731767

Stiffness optimization of non-linear elastic structures

M. Wallin, N. Ivarsson, D. A. Tortorelli

May 23, 2017

Computer Methods of Applied Mechanics and Engineering

Disclaimer

Stiffness optimization of non-linear elastic structures

Mathias Wallin[a,*], Niklas Ivarsson[a], Daniel Tortorelli[b]

[a] *Division of Solid Mechanics, Lund University, Box 118, SE-22100 Lund, Sweden*
[b] *Center for Design and Optimization, Lawrence Livermore National Laboratory, Livermore, CA, USA*

Abstract

This paper revisits stiffness optimization of non-linear elastic structures. Due to the non-linearity, several possible stiffness measures can be identified and in this work conventional compliance, i.e. secant stiffness designs are compared to tangent stiffness designs. The optimization problem is solved by the method of moving asymptotes and the sensitivities are calculated using the adjoint method. For the tangent cost function it is shown that although the objective involves the third derivative of the strain energy an efficient formulation for calculating the sensitivity can be obtained. Loss of convergence due to large deformations in void regions is addressed by using a fictitious strain energy such that small strain linear elasticity is approached in the void regions. A well-posed topology optimization problem is formulated by using restriction which is achieved via a Helmholtz type filter. The numerical examples provided show that for low load levels, the designs obtained from the different stiffness measures coincide whereas for large deformations significant differences are observed.

Keywords: Topology optimization, stiffness optimization, finite strains, non-linear elasticity

Introduction

Topology optimization has rapidly evolved and is now widely used in industry to create new innovative structural designs. The method is frequently used in the early design phase to find appropriate load paths wherein the goal is usually related to stiffness maximization as opposed to e.g. stress optimization, cf. [13]. The vast majority of the research on topology optimization is restricted to structures which operate in the linear regime, i.e. the deformations are assumed to be small and the material response linear. For an overview of the method and areas of applications see, [14]. To increase the range of applicability of the method, other cost functions and non-linear response should be considered.

For linear structures, the definition of the stiffness is well-defined since the tangent of the load-displacement response is independent of the load level, cf. Fig. 1a. However, for non-linear structures, the definition of the stiffness is not unique. One possible definition

*Division of Solid Mechanics, Lund University, Box 118, SE-22100 Lund, Sweden. E-mail: mathias.wallin@solid.lth.se

LLNL-ABS-731767
This work was partially performed under the auspices of the U.S. Department of Energy by Lawrence Livermore Laboratory under contract DE-AC52-07NA27344

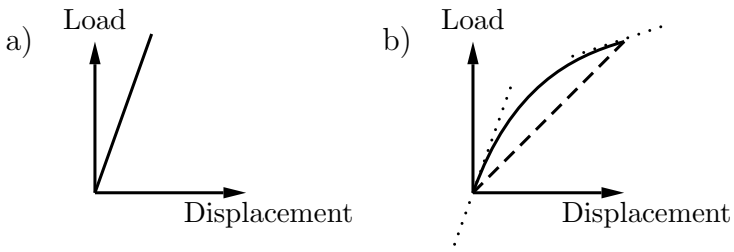

Figure 1: Illustration of stiffness for linear (a) and non-linear (b) materials. Initial and tangent stiffnesses are indicated via dotted lines; the secant stiffness is indicated via the dashed line.

uses the secant stiffness, i.e. the displacement under full load, as indicated by the dashed line in Fig. 1b. Another definition uses the strain energy of the structure, i.e. the area below the load-displacement graph. Yet another option uses the incremental, i.e. tangent, stiffness of the load-displacement response, cf. Fig. 1b which illustrates the initial and terminal stiffnesses via the dotted lines. It is interesting to note all these stiffness measures coincide for small strain linear elasticity. However, for nonlinear response this is certainly not the case. To further illustrate these differences, consider a structure that is close to a limit point, i.e. an infinitely small load increment will cause collapse of the structure, cf. Fig. 2. For this situation the secant stiffness is non-zero since both force and displacement

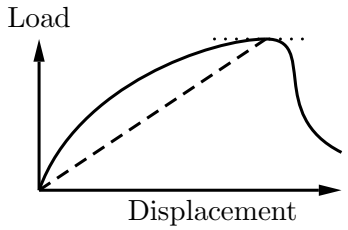

Figure 2: Illustration of stiffness at a limit point.

are positive. However, the tangent stiffness vanishes for a limit point since the slope of the load-displacement curve is zero.

Gradient based topology optimization requires the sensitivities of the cost and constraint functions. For linear elastic compliance optimization, the sensitivities are trivially computed. For non-linear materials and path-dependent materials, the sensitivity analyzes are more challenging, cf. e.g. [18]. To obtain the sensitivity, the adjoint procedure described in [10] is utilized in this work. As soon seen the combination of material non-linearity and the tangent stiffness cost function requires the third order derivative of the strain energy with respect to the displacement field. An efficient evaluation of this sensitivity is provided.

During the finite element simulations of the primal and adjoint responses it is well-known that the elements in low density regions become highly distorted causing convergence problems in the analyzes. Several remedies to this problem do exist, cf. e.g. [3] and [4]. In the present work the scheme based on a fictitious strain energy proposed in [19] is utilized such that the linear elasticity assumption is utilized in void regions, regardless of

the deformation.

The present work uses density based topology optimization with restriction to formulate a well-posed problem. The length-scale control is obtained via a Helmholtz filter as discussed in [12]. Moreover, to ensure that the final design is "crisp" we adopt a Heaviside thresholding method as discussed in [8]. The sensitivity is used to formulate a convex separable problem which is iteratively solved by the method of moving asymptotes (MMA), cf. [15]. Examples are provided to illustrate the differences between secant stiffness and tangent stiffness designs.

Preliminaries

To make the presentation transparent, we use both tensor and matrix notations. Bold faced times roman symbols e.g. $\boldsymbol{E}$ indicate vectors and tensors whereas bold sans serif symbols K indicate matrices. Lowercase superscripts e indicate quantities associated with finite element e. The sum $\sum\!\!\!\!\!\!\sum$ represents the usual finite element assembly.

Non-linear kinematics require that the current, i.e. deformed, configuration, Ω, needs to be distinguished from the reference, i.e. undeformed, configuration, Ω_o. Assuming elasto-statics, each material particle, identified by the position vector $\boldsymbol{X}$ in the reference configuration, Ω_o, is displaced to the position $\boldsymbol{x}$ in current configuration, Ω, by the smooth mapping $\boldsymbol{\varphi}$, i.e.

$$\boldsymbol{x} = \boldsymbol{\varphi}(\boldsymbol{X}) = \boldsymbol{u}(\boldsymbol{X}) + \boldsymbol{X}, \tag{1}$$

where $\boldsymbol{u}$ represents the displacement.The local deformation, i.e. strain, of the material is provided by the deformation gradient $\boldsymbol{F}$ such that

$$\boldsymbol{F} = \boldsymbol{\nabla}_o \boldsymbol{\varphi} = \mathbf{1} + \boldsymbol{\nabla}_o \boldsymbol{u}, \tag{2}$$

where $\boldsymbol{\nabla}_o$ represents the gradient with respect to the reference coordinates, $\boldsymbol{X}$ and $\mathbf{1}$ is the identity tensor. This mapping, $\boldsymbol{\varphi}$, from the reference configuration, Ω_o, to the current configuration, Ω, is assumed to be invertible, thus $J = det(\boldsymbol{F}) > 0$. Since the elastic material response only depends on the deformation of the material, the right Green-Cauchy deformation tensor $\boldsymbol{C}$ that is independent of rigid body motion is used in the material constitutive functions such that

$$\boldsymbol{C} = \boldsymbol{F}^T \boldsymbol{F}, \tag{3}$$

where $\boldsymbol{C} = \boldsymbol{C}(\boldsymbol{\nabla}_o \boldsymbol{u})$. And, for related reasons the Green-Lagrange strain tensor $\boldsymbol{E}$ is also introduced where

$$\boldsymbol{E} = \frac{1}{2}\left(\boldsymbol{C} - \mathbf{1}\right) = \frac{1}{2}\left(\boldsymbol{F}^T \boldsymbol{F} - \mathbf{1}\right). \tag{4}$$

Subsequently, a total Lagrangian formulation will be utilized and therefore the second Piola-Kirchhoff stress tensor, $\boldsymbol{S}$, is introduced as

$$\boldsymbol{S} = J \boldsymbol{F}^{-1} \boldsymbol{\sigma} \boldsymbol{F}^{-T}, \tag{5}$$

where $\boldsymbol{\sigma}$ is the Cauchy stress. In this way, neglecting body forces and inertia, equilibrium is locally described by

$$\boldsymbol{\nabla}_o \cdot (\boldsymbol{FS}) = \boldsymbol{0} \ \text{ in } \ \Omega_o, \tag{6}$$

where $\boldsymbol{\nabla}_o \cdot$ is the divergence operator with respect to the undeformed coordinates $\boldsymbol{X}$. The boundary conditions associated with (6), under the assumption of dead loading, are given by

$$\boldsymbol{FSn}_o = \bar{\boldsymbol{t}}^o \quad \text{on} \ \ \partial\Omega_{ot}, \ \ \boldsymbol{u} = \boldsymbol{\varphi} - \boldsymbol{X} = \boldsymbol{0} \ \text{on} \ \ \partial\Omega_{ou}, \tag{7}$$

where $\bar{\boldsymbol{t}}^o$ represents the prescribed traction and $\boldsymbol{n}_o$ is the outward unit normal vector to the boundary $\partial\Omega_o$. The complementary subsurfaces of $\partial\Omega_o$ where the traction and the displacement are prescribed are denoted $\partial\Omega_{ot}$ and $\partial\Omega_{ou}$, respectively.

To solve the above boundary value problem we use the principle of virtual work, i.e. we find the smooth $\boldsymbol{\varphi}$ that satisfies the Dirichlet boundary conditions on $\partial\Omega_{ou}$ and

$$r(\boldsymbol{\varphi}, \delta\boldsymbol{u}) = \int_{\Omega_o} \tilde{\boldsymbol{E}}(\boldsymbol{\varphi}, \delta\boldsymbol{u}) : \boldsymbol{S} dv - \int_{\partial\Omega_{ot}} \delta\boldsymbol{u} \cdot \bar{\boldsymbol{t}}^o dS = 0 \tag{8}$$

for all smooth virtual displacements $\delta\boldsymbol{u}$ that satisfy $\delta\boldsymbol{u} = \boldsymbol{0}$ on $\partial\Omega_{ou}$. In the above, the virtual Lagrangian strain $\tilde{\boldsymbol{E}}(\boldsymbol{\varphi}, \delta\boldsymbol{u})$, corresponding to $\delta\boldsymbol{u}$ is given by

$$\tilde{\boldsymbol{E}}(\boldsymbol{\varphi}, \delta\boldsymbol{u}) = \frac{1}{2}\left((\boldsymbol{\nabla}_o \delta\boldsymbol{u})^T \nabla_o \boldsymbol{\varphi} + (\nabla_o \boldsymbol{\varphi})^T \boldsymbol{\nabla}_o \delta\boldsymbol{u} \right). \tag{9}$$

For later purposes, we also note that a strain increment is expressed as

$$d\boldsymbol{E} = \tilde{\boldsymbol{E}}(\boldsymbol{\varphi}, d\boldsymbol{u}). \tag{10}$$

Constitutive model

The simplest finite strain elastic constitutive model valid for non-linear kinematics is the St. Venant strain energy function, defined as

$$W^{SV} = \frac{1}{2}\boldsymbol{E} : \mathbb{D}^{SV} : \boldsymbol{E}, \tag{11}$$

where $\mathbb{D}^{SV}$ is the fourth order small strain isotropic elastic tensor. However, it is well-known that the strain energy (11) does not adequately model material behavior for large strains, thus more realistic strain energy potential functions are needed. Nonetheless it was used in [2] to design structures and compliant mechanisms operating in the nonlinear regime.

An overview of strain energy potential functions used in topology optimization is provided in [11]. We use the isotropic compressible neo-Hookean model described in [17] wherein

$$W^{NH} = \frac{1}{2}K\left(\frac{1}{2}(J^2 - 1) - ln(J)\right) + \frac{1}{2}G\left(J^{-2/3} tr(\boldsymbol{C}) - 3\right), \tag{12}$$

where G and K in the limit of small strain correspond to the shear and bulk moduli, respectively.

Under our hyperelasticity assumption the second Piola Kirchhoff stress tensor is obtained from (12) as

$$\boldsymbol{S}(\boldsymbol{\nabla}_o \boldsymbol{u}) = 2\frac{\partial W^{NH}}{\partial \boldsymbol{C}} = \frac{1}{2}K(J^2-1)\boldsymbol{C}^{-1} + GJ^{-2/3}\left(\boldsymbol{1} - \frac{1}{3}\boldsymbol{C}^{-1}tr(\boldsymbol{C})\right). \tag{13}$$

The incremental stiffness tensor is defined by the second derivative of the strain energy with respect to the deformation tensor, i.e. $\mathbb{D} = 2\frac{\partial \boldsymbol{S}}{\partial \boldsymbol{C}}$ such that

$$\mathbb{D} = a_1\boldsymbol{C}^{-1}\otimes\boldsymbol{C}^{-1} + a_2\left(\boldsymbol{1}\otimes\boldsymbol{C}^{-1} + \boldsymbol{C}^{-1}\otimes\boldsymbol{1}\right) + a_3\left(\boldsymbol{C}^{-1}\underline{\otimes}\boldsymbol{C}^{-1} + \boldsymbol{C}^{-1}\overline{\otimes}\boldsymbol{C}^{-1}\right), \tag{14}$$

where the dyadic products $\underline{\otimes}$ and $\overline{\otimes}$ are defined such that $[\boldsymbol{A}\underline{\otimes}\boldsymbol{B}] : \boldsymbol{H} = \boldsymbol{A}\cdot\boldsymbol{H}^T\cdot\boldsymbol{B}^T$ and $[\boldsymbol{A}\overline{\otimes}\boldsymbol{B}] : \boldsymbol{H} = \boldsymbol{A}\cdot\boldsymbol{H}\cdot\boldsymbol{B}^T$ for second order tensors $\boldsymbol{A}$, $\boldsymbol{B}$ and $\boldsymbol{H}$ and the scalars a_1, a_2 and a_3 are given by

$$a_1 = \frac{2GJ^{-2/3}}{9}tr(\boldsymbol{C}) + KJ^2,\ a_2 = -\frac{2GJ^{-2/3}}{3},\ a_3 = \frac{J^{-2/3}G}{3}tr(\boldsymbol{C}) - \frac{K}{2}\left(J^2-1\right). \tag{15}$$

We call this the incremental elasticity tensor because

$$d\boldsymbol{S} = \mathbb{D} : d\boldsymbol{E}, \tag{16}$$

where we use the fact that $d\boldsymbol{E} = \frac{1}{2}d\boldsymbol{C}$.

For the ensuing sensitivity analysis we define the function

$$\begin{aligned} f_A(\boldsymbol{C}) &= \boldsymbol{A} : \mathbb{D}(\boldsymbol{C}) : \boldsymbol{A} \\ &= a_1(\boldsymbol{C})\left(tr(\boldsymbol{C}^{-1}\boldsymbol{A})\right)^2 + 2a_2(\boldsymbol{C})tr(\boldsymbol{A})tr(\boldsymbol{C}^{-1}\boldsymbol{A}) + 2a_3(\boldsymbol{C})tr(\boldsymbol{C}^{-1}\boldsymbol{A}\boldsymbol{C}^{-1}\boldsymbol{A}), \end{aligned} \tag{17}$$

and evaluate its gradient

$$\begin{aligned} \nabla f_A(\boldsymbol{C}) &= \left(tr(\boldsymbol{C}^{-1}\boldsymbol{A})\right)^2\nabla a_1(\boldsymbol{C}) + 2tr(\boldsymbol{A})tr(\boldsymbol{C}^{-1}\boldsymbol{A})\nabla a_2(\boldsymbol{C}) + 2tr(\boldsymbol{C}^{-1}\boldsymbol{A}\boldsymbol{C}^{-1}\boldsymbol{A})\nabla a_3(\boldsymbol{C}) - \\ &\quad 2\left(a_1(\boldsymbol{C})tr(\boldsymbol{C}^{-1}\boldsymbol{A}) + a_2(\boldsymbol{C})tr(\boldsymbol{A})\right)\boldsymbol{C}^{-1}\boldsymbol{A}\boldsymbol{C}^{-1} - 4a_3(\boldsymbol{C})\boldsymbol{C}^{-1}\boldsymbol{A}\boldsymbol{C}^{-1}\boldsymbol{A}\boldsymbol{C}^{-1}, \end{aligned} \tag{18}$$

where $\boldsymbol{A}$ is a second-order tensor and

$$\begin{aligned} \nabla a_1(\boldsymbol{C}) &= \left(KJ^2 - \tfrac{2GJ^{-2/3}}{27}tr(\boldsymbol{C})\right)\boldsymbol{C}^{-1} + \tfrac{2GJ^{-2/3}}{9}\boldsymbol{1} \\ \nabla a_2(\boldsymbol{C}) &= \tfrac{2G}{9}J^{-2/3}\boldsymbol{C}^{-1} \\ \nabla a_3(\boldsymbol{C}) &= -\left(\tfrac{KJ^2}{2} + \tfrac{J^{-2/3}G}{9}tr(\boldsymbol{C})\right)\boldsymbol{C}^{-1} + \tfrac{J^{-2/3}G}{3}\boldsymbol{1}\ . \end{aligned} \tag{19}$$

Total Lagrangian FE-formulation

The finite element formulation used herein is elementary and can be found in many text books (cf. e.g. [5]). However, since it will be extensively exploited in the sensitivity analysis it is illustrative to provide an overview. The starting point for the FE-formulation is the principle of virtual work (8) where we seek a $\mathbf{u}$ that approximates $\boldsymbol{u}$.

The approximated displacement field, $\mathbf{u}$, is interpolated in each finite element Ω_o^e using standard element polynomial shape functions $\mathbf{N}$, i.e. $\mathbf{u}(\boldsymbol{X}) = \mathbf{N}(\boldsymbol{X})\mathbf{a}^e$ where the $\mathbf{a}^e$ represent the element nodal degrees-of-freedom. The finite element formulation is based on the Galerkin approach, thus $\delta\mathbf{u}(\boldsymbol{X}) = \mathbf{N}(\boldsymbol{X})\delta\mathbf{a}^e$ where the virtual nodal degrees-of-freedom are denoted $\delta\mathbf{a}^e$. Inserting $\delta\mathbf{u}$ into the definition of $\tilde{\boldsymbol{E}}(\boldsymbol{\varphi}, \delta\boldsymbol{u})$ results in the discretized virtual strain which is expressed in Voigt notation as

$$\tilde{\mathbf{E}}(\mathbf{a}^e, \delta\mathbf{a}^e) = \mathbf{B}(\mathbf{a}^e)\delta\mathbf{a}^e, \tag{20}$$

where $\mathbf{B}(\mathbf{a}^e) = \mathbf{B}^c + \mathbf{B}^l(\mathbf{a}^e)$ is decomposed into a constant $\mathbf{B}^c$ and a linear $\mathbf{B}^l(\mathbf{a}^e)$ term, cf. [5] for details.

In the sensitivity analysis we will make use of the identity

$$\frac{\partial\left(\mathbf{B}(\mathbf{a}^e)\mathbf{w}\right)}{\partial\mathbf{a}^e} = \mathbf{B}^l(\mathbf{w}), \tag{21}$$

and for completeness, it is also noted that the Lagrangian strain in Voigt notation is computed from

$$\mathbf{E} = \left(\mathbf{B}^c + \frac{1}{2}\mathbf{B}^l(\mathbf{a}^e)\right)\mathbf{a}^e. \tag{22}$$

Using the arbitrariness of the virtual nodal displacements $\delta\mathbf{a}$, we define the residual vector

$$\mathbf{r}(\mathbf{a}, \lambda) = \mathbf{0} = \sum\int_{\Omega_o^e} \mathbf{B}^T(\mathbf{a}^e)\mathbf{S}dv - \lambda\mathbf{P} = \mathbf{F}_{int} - \lambda\mathbf{P}, \tag{23}$$

In the above the stress $\mathbf{S}$ is expressed in Voigt notation, and $\mathbf{P}$ is a unit magnitude external load so the load magnitude is given by the scalar load intensity factor, λ. As such, the equality $\mathbf{r}(\mathbf{a}, \lambda) = \mathbf{0}$ implies that $\mathbf{a}$ is an equilibrium state corresponding to the load intensity λ.

To find the solution to (23), the iterative Newton-Raphson scheme is used, i.e. in each iteration the increment of the nodal degrees-of-freedom $d\mathbf{a}$ is obtained from the solution to

$$\mathbf{K}d\mathbf{a} = -\mathbf{r}, \tag{24}$$

where the symmetric tangent stiffness matrix, $\mathbf{K} = \frac{\partial\mathbf{r}}{\partial\mathbf{a}}$, is given by

$$\mathbf{K} = \sum\int_{\Omega_o^e} \left(\mathbf{G}^T\mathbf{Y}\mathbf{G} + \mathbf{B}^T(\mathbf{a}^e)\mathbf{D}\mathbf{B}(\mathbf{a}^e)\right) dv, \tag{25}$$

where $\mathbf{G}$ contains the gradient of the element shape functions, $\mathbf{Y}$ is a symmetric block matrix that contains the stress and $\mathbf{D}$ the incremental stiffness expressed in Voigt notation.

The explicit formats of $\mathbf{G}$, $\mathbf{Y}$ and $\mathbf{B}$ are provided in the appendix and for details, we refer again to [5].

Equation (25) follows from the variation of the residual r evaluated at $(\boldsymbol{u}, \delta\boldsymbol{u})$ with respect to $\boldsymbol{u}$ in the direction $d\boldsymbol{u}$, i.e.

$$\delta_u r(\boldsymbol{u}, \delta\boldsymbol{u}; d\boldsymbol{u}) = \int_{\Omega_o} \Big(\tilde{\boldsymbol{E}}(d\boldsymbol{u}, \delta\boldsymbol{u}) : \boldsymbol{S} + \tilde{\boldsymbol{E}}(\boldsymbol{\varphi}, \delta\boldsymbol{u}) : \mathbb{D} : \tilde{\boldsymbol{E}}(\boldsymbol{\varphi}, d\boldsymbol{u}) \Big)\, dv, \tag{26}$$

where we use the relation $\delta\boldsymbol{\varphi}(\boldsymbol{X}) = \delta\boldsymbol{u}(\boldsymbol{X})$ and (16).

Filtration, restriction and projection

The design field z is parameterized to be piece-wise uniform over the finite elements Ω_o^e such that $z(\boldsymbol{X}) = z^e \in \{0, 1\}$ for $\boldsymbol{X} \in \Omega_o^e$. In this way, the design variable vector $\mathbf{z} = [z^1, z^2, \cdots]^T$ parameterizes the piece-wise uniform characteristic function that defines our optimized structure. However, it is well known that this parameterization cannot be used in the optimization as the resulting topology optimization problem is ill-posed. One way to make the optimization problem well-posed is to impose a length-scale restriction on $\mathbf{z}$ to prevent so-called chattering designs. We do this by implementing the partial differential equation (PDE) filter proposed in [9] and [12] and thus the piece-wise uniform characteristic function that defines our structure is replaced by the smooth field $\bar{\rho}$. Now that we have smeared the characteristic function, i.e. we generate regions on Ω_o which are neither purely material nor devoid of material, it does no harm to replace the discrete non-convex design space $z(\boldsymbol{X}) \in \{0, 1\}$ by a convex design space $z(\boldsymbol{X}) \in [0, 1]$ which enables derivative computations and thus the use of efficient gradient-based optimization algorithms to solve our topology optimization problem. To limit the effect of the smearing, we implement the thresholding and penalization strategies described below.

In the PDE filter the Helmholtz equation

$$-l_o^2 \Delta_o \bar{\rho} + \bar{\rho} = z \quad \text{in} \quad \Omega_o, \tag{27}$$

is solved subject to a body loading z and homogeneous flux boundary condition $\boldsymbol{\nabla}_o \bar{\rho} \cdot \boldsymbol{n}_o = 0$ on $\partial\Omega_o$. In the above Δ_o is the Laplacian with respect to the reference coordinates $\boldsymbol{X}$. The response field $\bar{\rho}$ serves as the volume fraction, i.e. density, that ultimately defines the optimized structure. Regions where $\bar{\rho}(\boldsymbol{X}) = 1$ and $\bar{\rho}(\boldsymbol{X}) = 0$ are either purely material or devoid of material. Regions where $\bar{\rho}(\boldsymbol{X}) \in (0, 1)$ contain mixtures which we reduce in size my implementing thresholding and penalization. The parameter $l_o > 0$ in (27) sets the filter length scale. Small l_o values admit designs with fine scale geometric variations and many holes. As l_o increases, such variations are inhibited yielding designs with smooth boundaries and fewer holes. It is also noted that $\bar{\rho}(\boldsymbol{X}) \in [0, 1]$ since $z(\boldsymbol{X}) \in [0, 1]$ and as a consequence of the divergence theorem and homogeneous Neumann boundary conditions, that $\int_{\Omega_o} \bar{\rho}\, dv = \int_{\Omega_o} z\, dv$, i.e. volume is conserved.

The PDE (27) is solved with the finite element method over the same mesh that is used in the mechanical analysis, i.e. the shape functions used in the interpolation of $\mathbf{u}$ are also

used to interpolate the filtered density $\bar{\rho}$ and weighting function $\delta\bar{\rho}$ in the residual equation

$$r_f(\bar{\rho}, \delta\bar{\rho}) = \int_{\Omega_o} \left(\boldsymbol{\nabla}_o \delta\bar{\rho} \cdot l_o^2 \boldsymbol{\nabla}_o \bar{\rho} + \delta\bar{\rho}(\bar{\rho} - z) \right) \, dv = 0 \tag{28}$$

which we solve for the smooth $\bar{\rho}$ for all smooth $\delta\bar{\rho}$. The details of the finite element analysis of (28) appear elsewhere (cf. [18]).Ultimately we compute $\bar{\boldsymbol{\rho}}$ from the matrix equation

$$\mathbf{K}_f \bar{\boldsymbol{\rho}} = \sum\!\!\!\!\!\!\int z^e \int_{\Omega_o^e} \mathbf{N}^T \, dv = \mathbf{P}_f \mathbf{z}, \tag{29}$$

where the elements of $\bar{\boldsymbol{\rho}}$ are the nodal values, i.e. degrees-of-freedom, that parameterize the filtered density field such that $\bar{\rho}(\boldsymbol{X}) = \mathbf{N}(\boldsymbol{X})\bar{\boldsymbol{\rho}}^e$ for $\boldsymbol{X} \in \Omega_o^e$ and

$$\mathbf{K}_f \;\; = \;\; \sum\!\!\!\!\!\!\int_{\Omega_o^e} \left(\boldsymbol{\nabla}_o \mathbf{N}^T \, l_o^2 \, \boldsymbol{\nabla}_o \mathbf{N} + \mathbf{N}^T \mathbf{N} \right) dv, \tag{30}$$

Since the finite element discretization is fixed, the symmetric, positive definite, matrix, $\mathbf{K}_f$ is fixed and consequently it only needs to be factored once. Moreover, since the columns $\sum\!\!\!\!\!\!\int_{\Omega_o^I} \mathbf{N}^T \, dv$ of the matrix $\mathbf{P}_f$ are constant it is also calculated once.

To reduce the size of the regions which are neither pure material nor devoid of material we implement the Heaviside thresholding technique, cf. [8]. In this method the filtered density field, $\bar{\rho}$ is mapped to $\rho \in \{0, 1\}$ using the Heaviside step function u_s. However, to avoid numerical difficulties due to the discontinuous Heaviside function a smoothed Heaviside function H, is employed such that

$$\rho = H(\bar{\rho}) = \frac{\tanh(\beta\omega) + \tanh(\beta(\bar{\rho} - \omega))}{\tanh(\beta\omega) + \tanh(\beta(1 - \omega))}, \tag{31}$$

where the parameters β and ω are such that $\lim_{\beta\to\infty} H(x) \to u_s(x - \omega)$. Notably, we still have regions in Ω_o which are neither pure material nor devoid of material since $\rho \in [0, 1]$. The above (31) approximation was introduced in [19], however in contrast to [19] where the threshold is applied to element quantities, here it is applied to the continuous field, $\bar{\rho}$.

To further reduce the size of the regions which are neither pure material nor devoid of material the thresholded density ρ is penalized via the SIMP scheme [1] wherein $\rho \mapsto \chi(\rho)$ such that

$$\chi(\rho) = \min(\rho^p, \delta_o), \tag{32}$$

where, as per usual, the minimum value δ_o is enforced to ensure that (8) is a well-posed structural problem. In the numerical examples the penalty exponent p is $p = 3$ and the bound is $\delta_o = 10^{-9}$.

As a result of all these mappings, the material response for each particle $\boldsymbol{X}$ is weighted by $\chi(\rho)$ such that

$$W = \chi(\rho) W^{NH}, \quad \boldsymbol{S} = 2\frac{\partial W}{\partial \boldsymbol{C}}, \quad \mathbb{D} = 2\frac{\partial \boldsymbol{S}}{\partial \boldsymbol{C}}. \tag{33}$$

In this way, we can think of χ as the indicator function. Indeed, as $\chi(\rho) \to 0$ the material behavior is extremely compliant to mimic void whereas as $\chi(\rho) \to 1$ the material behavior approaches that of the material which we are distributing, i.e. that with the energy function W^{NH}.

Summarizing, the "characteristic function" χ in (33) is obtained from the design field z via filtration, thresholding and penalization.

Optimization formulation

The optimization problem is stated as finding the design $\mathbf{z}$ that solves

$$\mathcal{P} \begin{cases} \min\limits_{\mathbf{z}} \; g_0(\mathbf{z}) \\ \\ \text{subject to} \begin{cases} g_1(\mathbf{z}) \leq 0 \\ \vdots \\ g_{n_c}(\mathbf{z}) \leq 0 \quad . \end{cases} \end{cases} \tag{34}$$

where g_0 is the "compliance" cost function to be minimized, or equivalently the "stiffness" to be maximized, and $g_i \leq 0$ are the n_c constraint inequalities to be satisfied. It is solved using a sequence of convex approximations which we describe below.

As discussed in the introduction, the "stiffness" is not unique for non-linear structures. A simple generalization from linear structures to non-linear structures is provided by minimizing the normalized work required to reach the deformed configuration. This "secant" optimization problem minimizes

$$g_0^s = \mathbf{P}^T \mathbf{a}, \tag{35}$$

where we recall that $\mathbf{P}$ is a unit vector.

Next, consider the stiffness defined from the tangent stiffness at the terminal state. To define the tangent stiffness consider again the residual equation (23). Expressing the nodal displacements as a function of the load intensity, λ, i.e. $\mathbf{a} = \mathbf{a}(\lambda)$, so that $\mathbf{r}(\mathbf{a}(\lambda), \lambda) = \mathbf{0}$, and linearizing (23) with respect to λ yields

$$\mathbf{K}\mathbf{v} - \mathbf{P} = \mathbf{0} \tag{36}$$

where $\mathbf{v} = \frac{\partial \mathbf{a}}{\partial \lambda}$. So maximizing the tangent stiffness at the load intensity λ is equivalent to minimizing $\mathbf{P}^T\mathbf{v}$. As such, the "tangent" optimization problem minimizes

$$g_0^t = \mathbf{P}^T \mathbf{v}. \tag{37}$$

We consider two kinds of constraints in our optimization problem. For all examples considered, the amount of available material is limited. This constraint is formulated as

$$g_1 = \int_{\Omega_0} H(\bar{\rho}) dv - V_{max} \leq 0, \tag{38}$$

where V_{max} is the maximum volume available for the design. In addition to the volume constraint, the displacement components a^α of individual nodes are constrained in several examples. These constraints are expressed as

$$g_2 = \mathbf{l}^T\mathbf{a} - d_{max} \leq 0, \tag{39}$$

where d_{max} is the maximum allowable displacement and $\mathbf{l}$ is defined such that $a^\alpha = \mathbf{l}^T\mathbf{a}$.

Sensitivity

The nonlinear optimization problem (34) is solved iteratively using the Method of Moving Asymptotes (cf. [15]). This algorithm uses the gradients of the cost and constraint functions to formulate a sequence of convex approximate sub-problems. As such, in each optimization iteration the load is incremented until the equilibrium is found for the terminal load intensity whence the sensitivity analysis commences. Motivated by the large number of design variables, the adjoint method is pursued to perform the sensitivity analysis. Below the sensitivities for both the secant and the tangent stiffness cost functions are derived.

Secant (s)

The sensitivity of (35) with respect to the filtered nodal density $\bar{\boldsymbol{\rho}}$ is derived by introducing the augmented function $\tilde{g}_0^s = \mathbf{P}^T\mathbf{a} - \boldsymbol{\eta}^T\mathbf{r}$ where $\boldsymbol{\eta}$ is the adjoint vector. Note that the augmented function equals the original function since $\mathbf{r} = \mathbf{0}$. Differentiation of $\tilde{g}_0^s$ and some rearranging results in

$$\frac{\partial \tilde{g}_0^s}{\partial \bar{\boldsymbol{\rho}}} = \left[\mathbf{P}^T - \boldsymbol{\eta}^T\mathbf{K}\right]\frac{\partial \mathbf{a}}{\partial \bar{\boldsymbol{\rho}}} - \boldsymbol{\eta}^T\frac{\partial \mathbf{r}}{\partial \bar{\boldsymbol{\rho}}}. \tag{40}$$

To eliminate the implicit derivative $\frac{\partial \mathbf{a}}{\partial \bar{\boldsymbol{\rho}}}$, $\boldsymbol{\eta}$ is taken as the solution to the linear adjoint problem

$$\mathbf{K}\boldsymbol{\eta} = \mathbf{P}. \tag{41}$$

Combining (23), (33), (40) and (41), results in the sensitivity

$$\frac{\partial g_0^s}{\partial \bar{\boldsymbol{\rho}}} = -\boldsymbol{\eta}^T\frac{\partial \mathbf{r}}{\partial \bar{\boldsymbol{\rho}}} = -\sum\int_{\Omega_o^e} \tilde{\mathbf{E}}(\boldsymbol{\eta}^e)^T\mathbf{S}\frac{\chi'}{\chi}H'\mathbf{N}^T dv \tag{42}$$

where we used $\frac{\partial \bar{\rho}}{\partial \bar{\boldsymbol{\rho}}} = \mathbf{N}^T$.

For the situation where the sensitivity of $g_2 = \mathbf{l}^T\mathbf{a} - d_{max}$ is required, we again use (42) however, $\boldsymbol{\eta}$ is obtained from the adjoint equation $\mathbf{K}\boldsymbol{\eta} = \mathbf{l}$.

To obtain the sensitivity with respect to the design variable $\mathbf{z}$ we use the chain rule whereby

$$\frac{\partial g_0^s}{\partial \mathbf{z}} = \frac{\partial g_0^s}{\partial \bar{\boldsymbol{\rho}}}\frac{\partial \bar{\boldsymbol{\rho}}}{\partial \mathbf{z}} = \left(\frac{\partial g_0^s}{\partial \mathbf{z}}\mathbf{K}_f^{-1}\right)\mathbf{P}_f \tag{43}$$

which follows from (29) and (42). Note that the above requires an additional back solve with the previously decomposed filter matrix $\mathbf{K}_f$ to compute $\frac{\partial g_0^s}{\partial \mathbf{z}}\mathbf{K}_f^{-1}$

The sensitivity of (43) could also be obtained by introducing the augumented function $\tilde{g}_0^s = \mathbf{P}^T\mathbf{a} - \boldsymbol{\eta}^T\mathbf{r} + \boldsymbol{\beta}^T(\mathbf{K}_f\bar{\boldsymbol{\rho}} - \mathbf{P}_f\mathbf{z})$ where $\boldsymbol{\eta}$ and $\boldsymbol{\beta}$ are adjoint vectors that are used to enforce the equilibrium and Helmholtz equations (8) and (29). Taking the derivative of this augumented function with respect to $\mathbf{z}$ and proceeding in the usual adjoint way, we would solve $\mathbf{K}\boldsymbol{\eta} = \mathbf{P}$ for $\boldsymbol{\eta}$ and then $\mathbf{K}_f\boldsymbol{\beta} = \left(\frac{\partial \mathbf{r}}{\partial \bar{\boldsymbol{\rho}}}\right)^T \boldsymbol{\eta}$ for $\boldsymbol{\beta}$ and finally evaluate the sensitivity $\frac{\partial g_0^s}{\partial \mathbf{z}} = -\boldsymbol{\beta}^T\mathbf{P}_f$, which, upon noting that $\boldsymbol{\beta} = \mathbf{K}_f^{-1}\left(\frac{\partial \mathbf{r}}{\partial \bar{\boldsymbol{\rho}}}\right)^T \boldsymbol{\eta}$ is equal to (43). This approach is advocated in [6, 7].

Tangent (t)

Whereas the sensitivity for the secant is almost trivial, the sensitivity for the tangent stiffness function is less straight forward. Following [10], the adjoint sensitivity analysis is based on the augmented function $\tilde{g}_0^t$ defined as

$$\tilde{g}_0^t = \mathbf{P}^T\mathbf{v} - \boldsymbol{\eta}^T\mathbf{r} - \boldsymbol{\mu}^T\left[\mathbf{K}\mathbf{v} - \mathbf{P}\right], \tag{44}$$

where $\boldsymbol{\eta}$ and $\boldsymbol{\mu}$ are the two adjoint vectors that enforce the equilibrium and incremental equilibrium equations (8) and (36). Again we note that the augmented function equals the original function since $\mathbf{r} = \mathbf{0}$ and $\mathbf{K}\mathbf{v} = \mathbf{P}$. Differentiating the augmented function (44) with respect to $\bar{\boldsymbol{\rho}}$ results in

$$\frac{d\tilde{g}_0^t}{d\bar{\boldsymbol{\rho}}} = -\left(\boldsymbol{\mu}^T\mathbf{K} - \mathbf{P}^T\right)\frac{\partial \mathbf{v}}{\partial \bar{\boldsymbol{\rho}}} - \left(\boldsymbol{\eta}^T\mathbf{K} + \frac{\partial}{\partial \mathbf{a}}\left(\boldsymbol{\mu}^T\mathbf{K}\mathbf{v}\right)\right)\frac{\partial \mathbf{a}}{\partial \bar{\boldsymbol{\rho}}} - \boldsymbol{\eta}^T\frac{\partial \mathbf{r}}{\partial \bar{\boldsymbol{\rho}}} - \frac{\partial}{\partial \bar{\boldsymbol{\rho}}}\left(\boldsymbol{\mu}^T\mathbf{K}\mathbf{v}\right) \tag{45}$$

To eliminate the influence of the implicit derivatives $\frac{d\mathbf{v}}{\partial \bar{\boldsymbol{\rho}}}$ and $\frac{d\mathbf{a}}{\partial \bar{\boldsymbol{\rho}}}$, the two adjoint vectors are chosen such that the terms in the parentheses in (45) vanish. First

$$\mathbf{K}\boldsymbol{\mu} = \mathbf{P} \tag{46}$$

is solved for the adjoint vector $\boldsymbol{\mu}$. But, since $\mathbf{v}$ is obtained from $\mathbf{K}\mathbf{v} = \mathbf{P}$, cf. (36), we see that $\boldsymbol{\mu}$ equals $\mathbf{v}$. Now that $\boldsymbol{\mu} = \mathbf{v}$ is known, the adjoint vector $\boldsymbol{\eta}$ is found from the solution to

$$\mathbf{K}\boldsymbol{\eta} = -\frac{\partial}{\partial \mathbf{a}}\left(\mathbf{v}^T\mathbf{K}\mathbf{v}\right), \tag{47}$$

which annihilates the second parentheses in (45). Substituting the adjoint vectors $\boldsymbol{\eta}$ and $\boldsymbol{\mu} = \mathbf{v}$ into (45) yields the sensitivity

$$\frac{dg_0^t}{d\bar{\boldsymbol{\rho}}} = -\boldsymbol{\eta}^T\frac{\partial \mathbf{r}}{\partial \bar{\boldsymbol{\rho}}} - \frac{\partial\left(\mathbf{v}^T\mathbf{K}\mathbf{v}\right)}{\partial \bar{\boldsymbol{\rho}}}. \tag{48}$$

To solve the adjoint problem (47) the adjoint load $\boldsymbol{\xi} = \frac{\partial}{\partial \mathbf{a}}\left(\mathbf{v}^T\mathbf{K}\mathbf{v}\right)$ needs to be evaluated. Using (25), we find

$$\boldsymbol{\xi} = \sum\!\!\!\!\!\!\int \frac{\partial}{\partial \mathbf{a}^e}\int_{\Omega_o^e}\left(\mathbf{v}^{eT}\mathbf{G}^T\mathbf{Y}\mathbf{G}\mathbf{v}^e + \mathbf{v}^{eT}\mathbf{B}^T(\mathbf{a}^e)\mathbf{D}\mathbf{B}(\mathbf{a}^e)\mathbf{v}^e\right)dv. \tag{49}$$

Expanding the diagonal blocks in $\mathbf{Y}$ and making use of (10) and (16) yields

$$\frac{\partial}{\partial \mathbf{a}^e}\left(\mathbf{v}^{eT}\mathbf{G}^T\mathbf{Y}\mathbf{G}\mathbf{v}^e\right) = \mathbf{B}(\mathbf{a}^e)^T\mathbf{D}\tilde{\mathbf{E}}(\mathbf{v}^e,\mathbf{v}^e).$$

Furthermore, considering the second term in (49), differentiating, while keeping the stiffness, $\mathbf{D}$, fixed and using the identity (21) results in

$$\frac{\partial}{\partial \mathbf{a}^e}\left(\mathbf{v}^{eT}\mathbf{B}^T(\mathbf{a}^e)\hat{\mathbf{D}}\mathbf{B}(\mathbf{a}^e)\mathbf{v}^e\right)|_{\hat{\mathbf{D}}=\mathbf{D}(\mathbf{a}^e)} = 2\ \mathbf{B}^l(\mathbf{a}^e)^T\mathbf{D}\tilde{\mathbf{E}}(\mathbf{a}^e,\mathbf{v}^e).$$

The last part of the adjoint load is obtained from again differentiating the second term in (49) but keeping $\mathbf{B}$ fixed and using (18) with $\boldsymbol{\nabla}_o\boldsymbol{v}$ replacing $\boldsymbol{A}$, i.e.

$$\frac{\partial}{\partial \mathbf{a}^e}\left(\mathbf{v}^{eT}\hat{\mathbf{B}}^T\mathbf{D}(\mathbf{a}^e)\hat{\mathbf{B}}\mathbf{v}^e\right)|_{\hat{\mathbf{B}}=\hat{\mathbf{B}}(\mathbf{a}^e)} = \mathbf{B}(\mathbf{a}^e)^T 2\nabla \mathsf{f}_{\nabla \mathsf{v}}(\mathbf{C}).$$

where $\boldsymbol{\nabla}\mathsf{v} = \mathbf{B}\mathbf{v}^{\mathbf{e}}$ and $\nabla \mathsf{f}_{\nabla \mathsf{v}}$ are expressed in Voigt notation. Combining the identities above, we express the adjoint load vector as

$$\boldsymbol{\xi} = \sum\!\!\!\!\!\!\int_{\Omega_o^e}\left[\mathbf{B}(\mathbf{a}^e)^T\left(\mathbf{D}\tilde{\mathbf{E}}(\mathbf{v}^e,\mathbf{v}^e)) + 2\nabla \mathsf{f}_{\nabla \mathsf{v}}(\boldsymbol{C})\right) + 2\ \mathbf{B}^{lT}(\mathbf{v}^e)\mathbf{D}\tilde{\mathbf{E}}(\mathbf{a}^e,\mathbf{v}^e)\right] dv \tag{50}$$

Alternatively, we also note that the $\boldsymbol{\xi}$ follows from the second residual variation at $\boldsymbol{u}$ and $\boldsymbol{v}$ acting in the directions $\boldsymbol{v}$ and $\delta\boldsymbol{u} = \frac{d\boldsymbol{u}}{d\bar{\rho}^\alpha}$, i.e. $\delta^2 r(\boldsymbol{u},\boldsymbol{v};\boldsymbol{v},\delta\boldsymbol{u})$.

It is noted that the adjoint load vector (50) has a structure similar to the residual (23) and can be evaluated at the element level using the standard finite element assembly process.

The last part of the sensitivity analysis is to evaluate (48), i.e.

$$\frac{\partial g_0^t}{\partial \bar{\boldsymbol{\rho}}} = -\sum\!\!\!\!\!\!\int_{\Omega_o^e}\left(\tilde{\mathbf{E}}(\mathbf{a}^e,\boldsymbol{\eta}^e)^T\mathbf{S} + \mathbf{v}^{eT}\mathbf{G}^T\mathbf{Y}\mathbf{G}\mathbf{v}^e + \tilde{\mathbf{E}}(\mathbf{a}^e,\mathbf{v}^e)^T\mathbf{D}\tilde{\mathbf{E}}(\mathbf{a}^e,\mathbf{v}^e)\right)\frac{\chi'}{\chi}H'\mathbf{N}^T dv \tag{51}$$

The chain rule of (43) is similarly used to obtain $\frac{\partial g_0^t}{\partial \mathbf{z}}$.

The pseudo code for updating the design for the tangent sensitivity cost function is provided in Box 1.

Highly distorted elements

To avoid convergence problems associated with highly distorted elements in void regions the approach presented in [19] will be utilized. It is based on the idea that void regions have negliable influence on the response and therefore the physical strain energy in these regions can be substituted by any suitable approximation. To these ends, in regions with full material, the strain energy is the physical strain energy, here W^{NH}, whereas in void regions the linearized strain energy $W^L(\rho,\boldsymbol{\nabla}_o\boldsymbol{u}) = \frac{1}{2}\boldsymbol{\epsilon} : \mathbb{D}^L : \boldsymbol{\epsilon}$ is used where $\boldsymbol{\epsilon}(\boldsymbol{\nabla}_o\boldsymbol{u}) = \frac{1}{2}(\boldsymbol{\nabla}_o\boldsymbol{u} + (\boldsymbol{\nabla}_o\boldsymbol{u})^T)$ is the infinitesimal strain tensor.

· Solve mechanical balance laws until $\lambda = \lambda_N$

Increase load level $\lambda_{i+1} := \lambda_i + \Delta\lambda$

Perform Newton equilibrium iterations until $\mathbf{r}(\mathbf{a}, \lambda_{i+1}) = \mathbf{0}$

· Solve $\mathbf{K}\mathbf{v} = \mathbf{P}$ for incremental displacement $\mathbf{v}$

· Evaluate $g^T = \mathbf{v}^T\mathbf{P}$

· Sensitivity analysis:

Calculate adjoint force $\boldsymbol{\xi} = \frac{\partial}{\partial \mathbf{a}}\left(\mathbf{v}^T\mathbf{K}\mathbf{v}\right)$, cf. (50)

Solve $\mathbf{K}\boldsymbol{\eta} = \boldsymbol{\xi}$ for the adjoint vector $\boldsymbol{\eta}$

Calculate the sensitivity $\frac{\partial g_0^t}{\partial \bar{\boldsymbol{\rho}}} = -\boldsymbol{\eta}^T \frac{\partial \mathbf{r}}{\partial \bar{\boldsymbol{\rho}}} - \frac{\partial\left(\mathbf{v}^T\mathbf{K}\mathbf{v}\right)}{\partial \bar{\boldsymbol{\rho}}}$, cf. (51)

Solve $\mathbf{K}_f\mathbf{y} = \frac{\partial g_0^t}{\partial \bar{\boldsymbol{\rho}}}$ for $\mathbf{y}$ and evaluate $\frac{\partial g_0^t}{\partial \mathbf{z}} = \mathbf{P}_f^T\mathbf{y}$, cf. (43)

Box 1: Summary of tangent stiffness and tangent stiffness sensitivity evaluations.

To smoothly transition between W^{NH} and W^L, a scalar variable γ is used. It should be noted that in contrast to [19] where γ is evaluated as piece-wise uniform over the finite elements, γ is in this work a continous field variable that is related to the continuous density ρ via the smoothed Heaviside approximation

$$\gamma = \frac{\tanh\left(\beta_1\,\rho_o\right) + \tanh\left(\beta_1\,\left(\rho^p - \rho_o\right)\right)}{\tanh\left(\beta_1\,\rho_o\right) + \tanh\left(\beta_1\,\left(1 - \rho_o\right)\right)} \tag{52}$$

where the smoothening parameters $\beta_1 = 500$ and $\rho_o = 0.01$ are chosen in accordance with [19] and kept constant in all simulations, cf. the discussion following (31), Ultimately the strain energy in (33) is replaced by

$$W(\rho, \boldsymbol{\nabla}_o\boldsymbol{u}; \gamma) = W^{NH}(\rho, \gamma\boldsymbol{\nabla}_o\boldsymbol{u}) - W^L(\rho, \gamma\boldsymbol{\nabla}_o\boldsymbol{u}) + W^L(\rho, \boldsymbol{\nabla}_o\boldsymbol{u}). \tag{53}$$

Clearly, for $\rho = 1$ we have $\gamma = 1$ so that $W = W^{NH}$ whereas for $\rho = 0$ we have $\gamma = 0$ so that $W = W^L$.

Numerical examples

The presented algorithm is used to solve two topology optimization problems. In both cases, the MMA algorithm updates the design using the default MMA parameters, cf. [15]. Although the problems are planar, 3D 8-node displacement based fully integrated elements are utilized. The elastic parameters in all examples are chosen as $E = 3$GPa and $\nu = 0.4$ which provide $G = E/(2(1+\nu))$ and $K = E/3(1-2\nu)$. Plane strain is simulated which

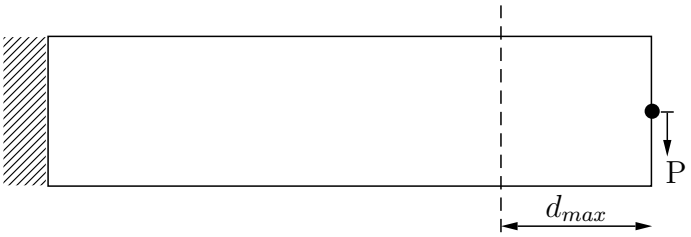

Figure 3: Design domain and boundary conditions used in the cantilever beam example. The dashed line indicates the maximum horizontal displacement used in the tangent example.

implies the displacement in the out-of-plane direction is zero. The filter radius is chosen as $l_o = 20$mm, cf. (27) and the load intensity increment is chosen such that 4-9 load steps are required for the analysis. A continuation scheme for the penalty factor, p, is utilized wherein the initial value of $p = 2$ is increased to the final value $p = 3$ in increments of 0.05 every 5 design updates. After the terminal value $p = 3$ is reached, the Heaviside parameter β is increased from $\beta = 1$ to $\beta = 40$ in increments of 1 every 10 design updates. The parameter ω is fixed at $\omega = 0.5$ in all simulations.

Cantilever beam

As a base line we optimize the perverbial cantilever beam. The beam length, width and out-of-plane tickness are 4000mm and 1000mm and 100mm, cf. Fig. 3. The structure is discretized using 120x30 8-node elements with one element used through the thickness. The maximum allowed volume is 50% of the design domain volume in the reference configuration.

First, the structure is optimized using the secant cost function for different load intensities, λ. The results illustrated in Fig. 4 visually resembles those in [19] where it is seen that the finite element formulation along with the optimization scheme are able to accomondate very large deformations. As previously reported, cf. e.g. [16], secant optimimzation of cantilever beams results in designs with cable-like segments.

Now, the cantilever beam is optimimzed with respect to the tangent cost function. Since the tangent function does not inherently impose a restriction on the displacement the optimization will strive to align the structure in the load direction, i.e. a design where the deformed beam is rotated 90 degrees is approached by introducing a "hinge" at the clamped edge. However, to enforce a beam-like structure the end-stiffness cost function will be combined with a constraint on the horizontal displacement. To this end the node where the load is applied cannot deform more than d_{max} in the horizontal direction. In the examples presented below this limit is chosen as $d_{max} = 300$mm, i.e. the load point is allowed to move 30% of the beam's length. To summarize, the tangent problem is

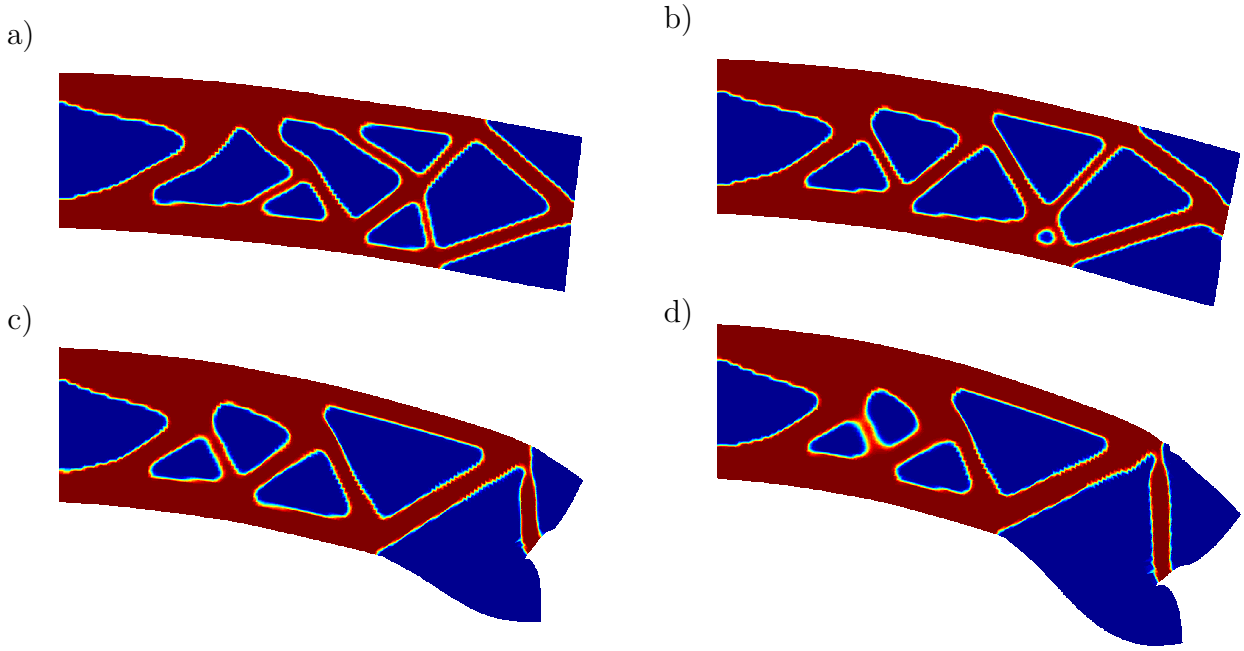

Figure 4: The optimized designs for four different load intensities using the secant cost function. The applied load intensity are a) 100kN, b) 150kN, c) 200kN and d) 300kN.

fomulated as:

$$\mathcal{P}\left\{\begin{array}{l} \underset{\mathbf{z}}{min}\ g_0^t \\ \\ \text{subject to}\left\{\begin{array}{l} g_1 = \int_{\Omega_0} H(\bar{\rho})dv - V_{max} \leq 0 \\ g_2 = \mathbf{l}^T\mathbf{a} - d_{max} \leq 0\ . \end{array}\right. \end{array}\right. \tag{54}$$

In Fig. 5, the optimized designs are shown for different load intensities. In all designs, the horizontal displacement constraint is active and a hinge is created. This hinge feature appears because the vertical displacement has no influence on this tangent cost versus the secant cost function.

Fig. 6 shows the effect of the energy scaling. As reported in [19], the scheme is able to accomondate extremly large distortions and in some cases the deformed finite element mesh contains overlapping elements in the void region.

To further illustrate the difference between the cost functions, the load-displacement response for the 250kN load is considered, cf. Fig. 7. As expected, the optimal design using the secant cost function results in less vertical displacement whereas the optimized design using the tangent cost function results in a steeper terminal load-displacement curve, i.e. a greater incremental stiffness.

Finally, the two formulations are compared for a small $1kN$ load, cf. Fig. 8, where it is seen that the designs are almost identical and that the horizontal displacement constraint is not active. This is expected since the designs are effectively operating in the linear regime.

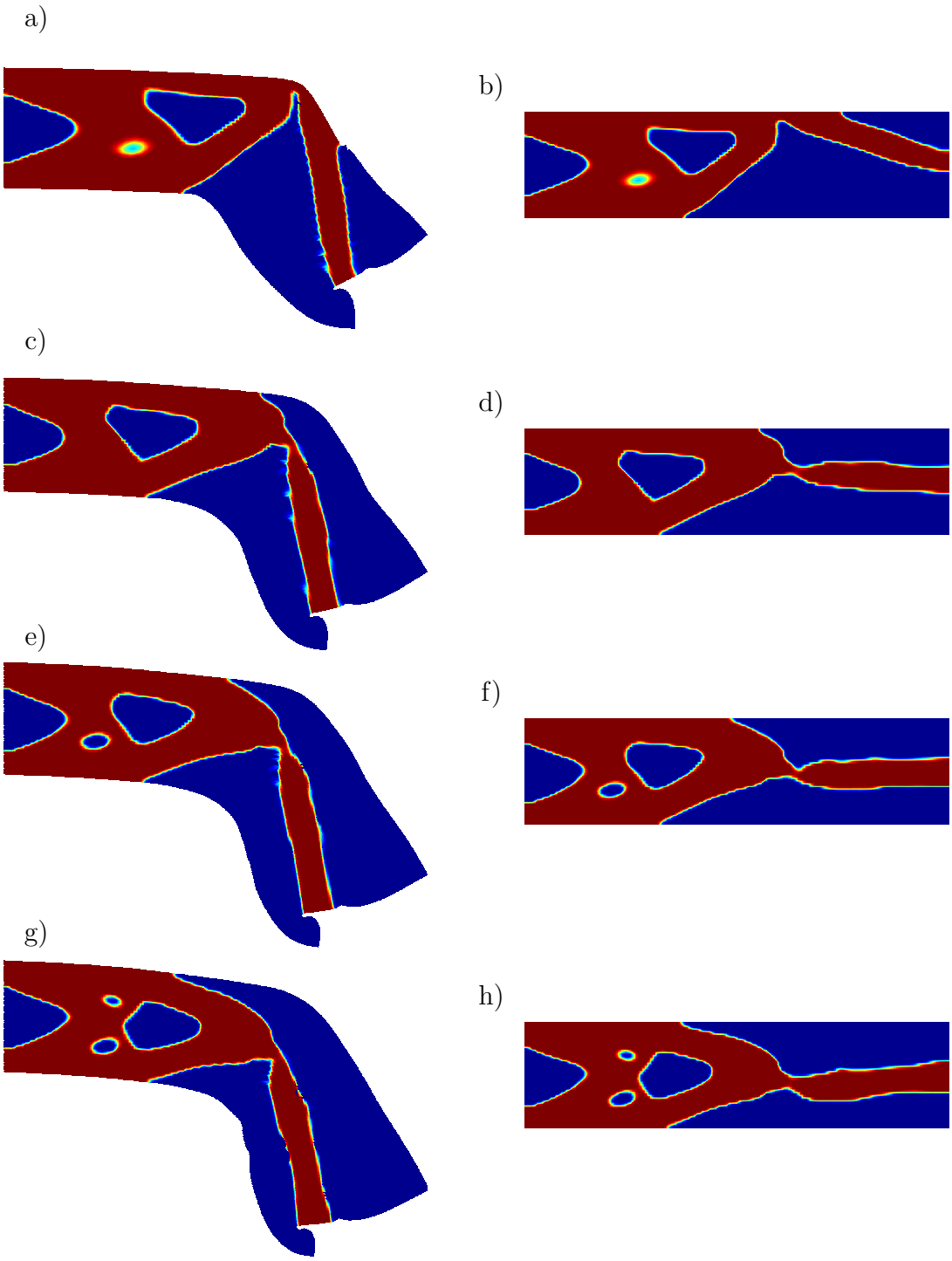

Figure 5: The optimized designs in the deformed (left) and undeformed (right) configurations for three different load intensities using the tangent cost function. (a-b) 100kN, (c-d) 150kN, (e-f) 200kN and (g-h) 250kN.

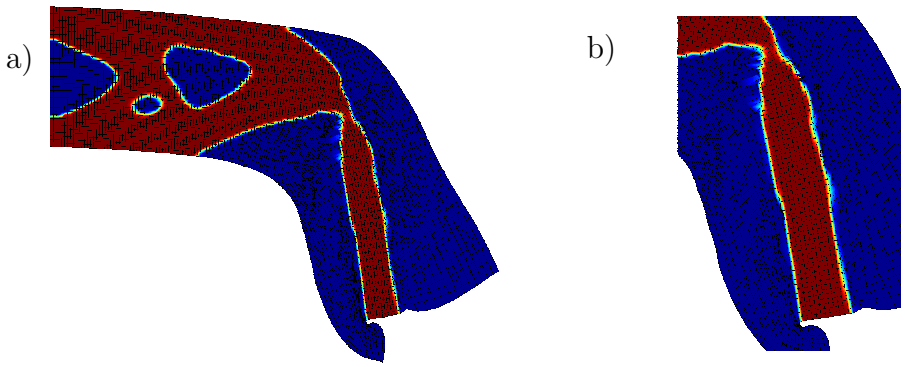

Figure 6: The optimized design in the deformed configuration for 200kN a) and b) close up of finite element mesh in the vicinity of the hinge.

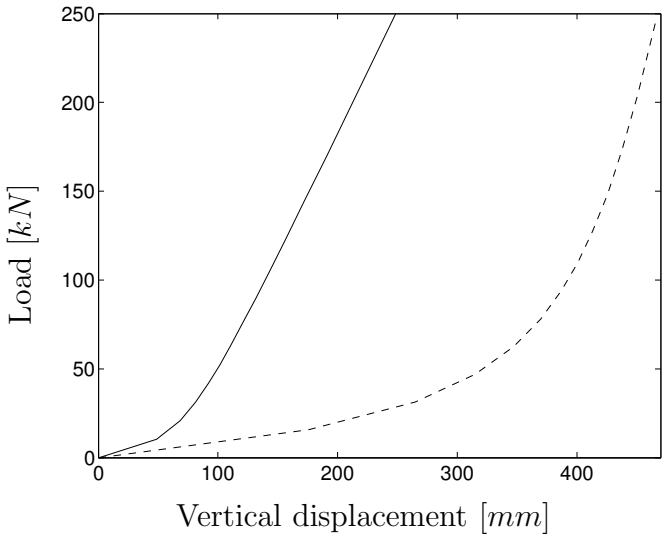

Figure 7: Load-displacement response for the optimized 250kN design using the secant (solid line) and tangent (dashed line) cost functions.

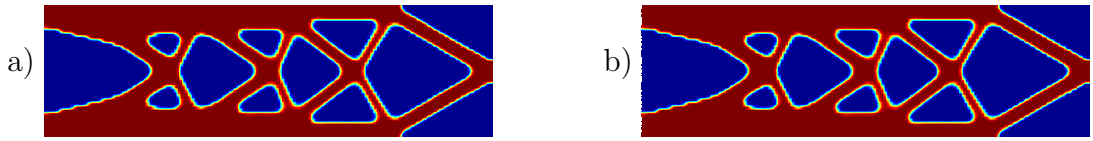

Figure 8: The optimized designs for the $1kN$ load for a) the secant cost and b) tangent cost functions.

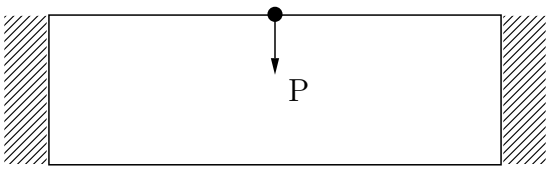

Figure 9: Design domain and boundary conditions used in the double clamped beam example.

Double clamped beam

To further highlight the difference beween the secant and the tangent cost functions the double clamped beam, illustrated in Fig. 9, is considered. The length, width and out-of-plane thickness of the beam are 6000mm and 1000mm and 100mm. The maximum allowed volume for the design is 10% of the volume of the design domain in the reference configuration as done in [19]. All other material and numerical parameters are the same as in the previous example. The material is initially randomly distributed, however, to trigger a V-shaped optimized structure and thereby avoid snap-through, the initial distribution is slighly pertubed such that a V-type structure favored. The structure can be simulated without domain symmetry conditions, however, the tangent stiffness design for this case will generate a structure that is similar to the cantilever beam example, i.e. detatched at one end and aligned with the load direction at the other end. To eliminate this possibility, symmetry is enforced. Fig. 10 illustrates the optimal designs for both the secant and the tangent stiffness cost functions corresponding to a $500kN$ load. Again, as expected the design optimized for minimal secant results in less deformation whereas the tangent design has a greater incremental stiffness, cf. Fig. 11.

Conclusion

In this paper, finite strain topology optimimzation that considers tangent stiffness has been developed. Although the cost function involves the third order derivative of the strain energy potential a compact and efficient numerical scheme for the sensitivity analysis is developed. Numerical examples show significant differences between designs obtained using the tangent and secant cost functions.

Acknowledgements

This work performed under the auspices of the U.S. Department of Energy by Lawrence Livermore Laboratory under Contract DE-AC52-07NA27344. The financial support from the Swedish research council (grant ngb. 2015-05134) is also gratefully acknowledged. The authors would also like to thank Professor Krister Svanberg for providing the MMA code.

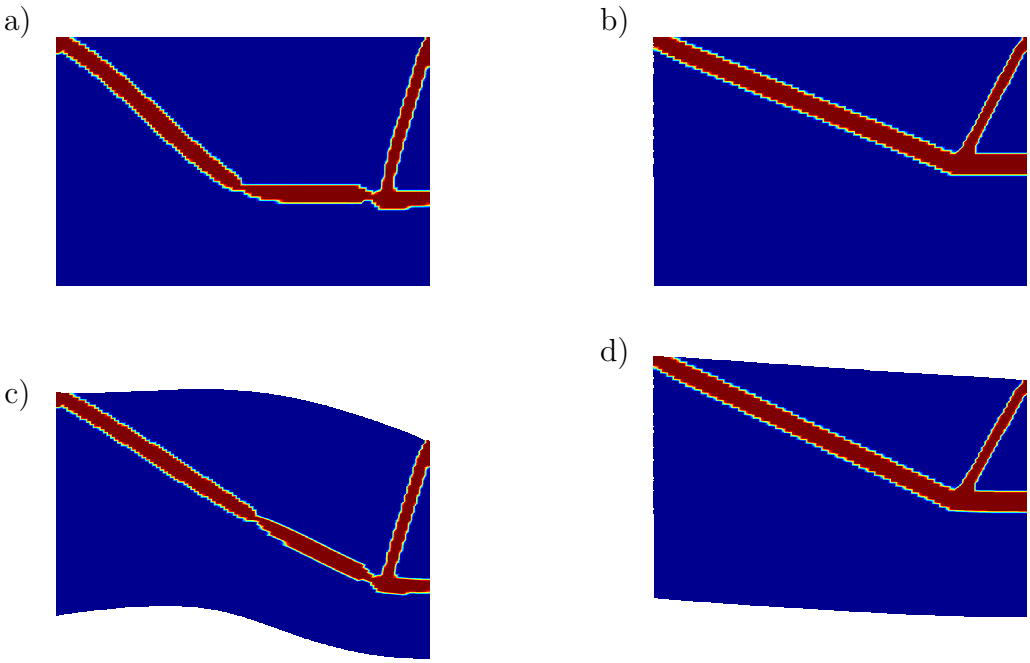

Figure 10: Undeformed and deformed optimized designs for the tangent (a) and (c) and secant (b) and (d) cost functions.

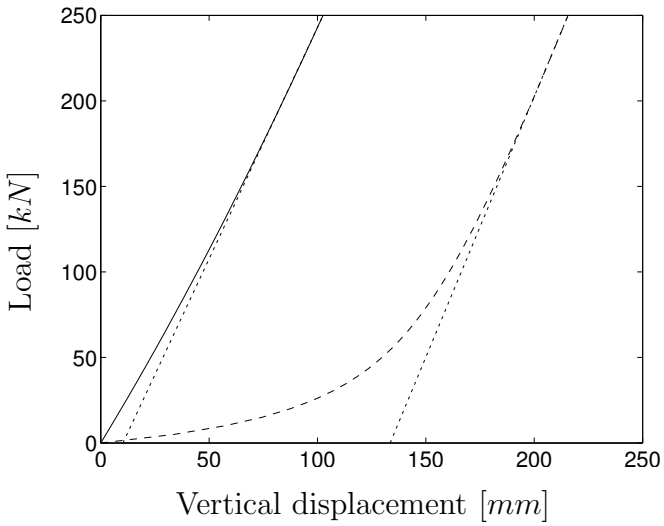

Figure 11: Load-displacement response for the optimized design using the secant (solid line) and tangent (dashed line) cost functions. The tangents to the load displacement graphs at the terminal load are indicated by dotted lines.

References

[1] Martin P Bendsøe. Optimal shape design as a material distribution problem. *Structural optimization*, 1(4):193–202, 1989.

[2] T E. Bruns and D. A. Tortorelli. Topology optimization of non-linear elastic structures and compliant mechanisms. *Comput. Methods Appl. Mech. Engng.*, 190:3443–3459, 2001.

[3] TE Bruns and DA Tortorelli. An element removal and reintroduction strategy for the topology optimization of structures and compliant mechanisms. *International Journal for Numerical Methods in Engineering*, 57(10):1413–1430, 2003.

[4] Thomas Buhl, Claus BW Pedersen, and Ole Sigmund. Stiffness design of geometrically nonlinear structures using topology optimization. *Structural and Multidisciplinary Optimization*, 19(2):93–104, 2000.

[5] M. A. Crisfield. *Non-linear Finite Element Analysis of Solids and Structures*, volume 1. Wiley, 1991.

[6] Yongbo Deng and Jan G. Korvink. Topology optimization for three-dimensional electromagnetic waves using an edge element-based finite-element method. *Proceedings of the royal society A Mathematical physical and engineering sciences*, 472(2189), 2016.

[7] Yongbo Deng, Zhenyu Liu, Yongshun Liu, and Yihui Wu. Combination of topology optimization and optimal control method. *Journal of Computational Physics*, 257(A):374–399, JAN 15 2014.

[8] James K Guest, Jean H Prévost, and T Belytschko. Achieving minimum length scale in topology optimization using nodal design variables and projection functions. *International Journal for Numerical Methods in Engineering*, 61(2):238–254, 2004.

[9] Atsushi Kawamoto, Tadayoshi Matsumori, Shintaro Yamasaki, Tsuyoshi Nomura, Tsuguo Kondoh, and Shinji Nishiwaki. Heaviside projection based topology optimization by a PDE-filtered scalar function. *Structural and Multidisciplinary Optimization*, 44(1):19–24, 2011.

[10] R Kemmler, A Lipka, and E Ramm. Large deformations and stability in topology optimization. *Structural and Multidisciplinary Optimization*, 30(6):459–476, 2005.

[11] A. Klarbring and N. Strömberg. Topology optimization of hyperelastic bodies including non-zero prescribed displacements. *Struct. Multidisc. Optim.*, 47(1):37–48, 2013.

[12] B. S. Lazarov and O. Sigmund. Filters in topology optimization based on helmholtz-type differential equations. *Int. J. Numer. Meth. Engng.*, 86(6):765–781, 2011.

[13] C. Le, J. Norato, T. Bruns, C. Ha, and D. Tortorelli. Stress-based topology optimization for continua. *Struct. Multidisc. Optim.*, 41:87–106, 2010.

[14] Ole Sigmund and Kurt Maute. Topology optimization approaches. *Structural and Multidisciplinary Optimization*, 48(6):1031–1055, 2013.

[15] K. Svanberg. The method of moving asymptotes- a new method for structural optimization. *Int. J. Numer. Meth. Engng.*, 24:359–373, 1987.

[16] M. Wallin and M. Ristinmaa. Finite strain topology optimization based on phase-field regularization. *Struct. Multidisc. Optim.*, pages 1–13, 2014.

[17] Mathias Wallin, Niklas Ivarsson, and Matti Ristinmaa. Large strain phase-field based multi-material topology optimization. *International Journal for Numerical Methods in Engineering*, 2015.

[18] Mathias Wallin, Viktor Jönsson, and Eric Wingren. Topology optimization based on finite strain plasticity. *Structural and Multidisciplinary Optimization*, pages 1–11, 2016.

[19] Fengwen Wang, Boyan Stefanov Lazarov, Ole Sigmund, and Jakob Søndergaard Jensen. Interpolation scheme for fictitious domain techniques and topology optimization of finite strain elastic problems. *Comput. Methods Appl. Mech. Engng.*, 276:453–472, 2014.

Appendix

The matrices entering the geometric part of the stiffness matrix $\mathbf{K}$, cf. (25) are defined as

$$\mathbf{G} = \begin{bmatrix} \underbrace{\begin{matrix} N_{1,x} & 0 & 0 \\ N_{1,y} & 0 & 0 \\ N_{1,z} & 0 & 0 \\ 0 & N_{1,x} & 0 \\ 0 & N_{1,y} & 0 \\ 0 & N_{1,z} & 0 \\ 0 & 0 & N_{1,x} \\ 0 & 0 & N_{1,y} \\ 0 & 0 & N_{1,z} \end{matrix}}_{node1} & \ldots & \underbrace{\begin{matrix} N_{8,x} & 0 & 0 \\ N_{8,y} & 0 & 0 \\ N_{8,z} & 0 & 0 \\ 0 & N_{8,x} & 0 \\ 0 & N_{8,y} & 0 \\ 0 & N_{8,z} & 0 \\ 0 & 0 & N_{8,x} \\ 0 & 0 & N_{8,y} \\ 0 & 0 & N_{8,z} \end{matrix}}_{node8} \end{bmatrix} \quad \mathbf{Y} = \begin{bmatrix} \mathbf{S}_{3x3} & \mathbf{0} & \mathbf{0} \\ \mathbf{0} & \mathbf{S}_{3x3} & \mathbf{0} \\ \mathbf{0} & \mathbf{0} & \mathbf{S}_{3x3} \end{bmatrix}$$

where we have assumed 8 node brick elements. The matrix $\mathbf{S}_{3x3}$ represents the 3 by 3 matrix representation of the second Piola-Kirchhoff stress tensor. The discrete strain operator $\mathbf{B}$ is decomposed in $\mathbf{B} = \mathbf{B}^c + \mathbf{B}^l$ where the linear part is given by

$$\mathbf{B}^l(\mathbf{a}^e) = \begin{bmatrix} u_{x,x} & 0 & 0 & u_{y,x} & 0 & 0 & u_{z,x} & 0 & 0 \\ 0 & u_{x,y} & 0 & 0 & u_{y,y} & 0 & 0 & u_{z,y} & 0 \\ 0 & 0 & u_{x,z} & 0 & 0 & u_{y,z} & 0 & 0 & u_{z,z} \\ u_{x,y} & u_{x,x} & 0 & u_{y,y} & u_{y,x} & 0 & u_{z,y} & u_{z,x} & 0 \\ u_{x,z} & 0 & u_{x,x} & u_{y,z} & 0 & u_{y,x} & u_{z,z} & 0 & u_{z,y} \\ 0 & u_{x,z} & u_{x,y} & 0 & u_{y,z} & u_{y,y} & 0 & u_{z,z} & u_{z,y} \end{bmatrix} \mathbf{G}$$

and the constant part is given by

$$\mathbf{B}^c = \begin{bmatrix} \underbrace{\begin{matrix} N_{1,x} & 0 & 0 \\ 0 & N_{1,y} & 0 \\ 0 & 0 & N_{1,z} \\ N_{1,y} & N_{1,x} & 0 \\ N_{1,z} & 0 & N_{1,x} \\ 0 & N_{1,z} & N_{1,y} \end{matrix}}_{node1} & \cdots & \underbrace{\begin{matrix} N_{8,x} & 0 & 0 \\ 0 & N_{8,y} & 0 \\ 0 & 0 & N_{8,z} \\ N_{8,y} & N_{8,x} & 0 \\ N_{8,z} & 0 & N_{8,x} \\ 0 & N_{8,z} & N_{8,y} \end{matrix}}_{node8} \end{bmatrix}$$